

Article

Critical Comparison of Li-Ion Aging Models for Second Life Battery Applications

Sai Vinayak Ganesh and Matilde D'Arpino * 

Department of Mechanical and Aerospace Engineering, The Ohio State University, Columbus, OH 43214, USA

* Correspondence: darpino.2@osu.edu

Abstract: Lithium-ion batteries (LIBs) from electrified vehicles (EVs) that have reached the automotive end of life (EoL) may provide a low-cost, highly available energy storage solution for grid-connected systems, such as peak shaving and ancillary services. There are several issues related to the integration of second life batteries (SLBs) in power systems, such as the variability of the pack design and cell chemistry, in-field assessments of the state of health (SoH), and estimations of the expected lifetimes of SLBs in different power system applications. Model-based approaches are commonly used in the automotive industry for estimating/predicting the capacity and power fade trajectories of LIBs during their life. However, a large variety of models are available with different fidelities, complexities, and computational costs. The accuracy of these estimations is critical for the derivation of business models for SLB applications. This paper presents a qualitative and quantitative assessment of the performance of two well-accepted, state-of-the-art aging models, initially developed for automotive applications and here applied to different SLB applications to predict both the capacity and power fade. These models are evaluated with respect to several performance metrics, such as fidelity of estimation and capability of extrapolation outside the calibration data range. The considered models are classified as semi-empirical physics-based and empirical models, respectively. Three different SLB power profiles, bulk energy for DC fast charge stations and two frequency regulation profiles, are considered, corresponding to different ranges of the SoC, C-rates, and battery temperatures, with the aim of exciting different aging mechanisms. The numerical results provide insight for the selection of aging models for SLB applications based on their performances and limitations.



Citation: Ganesh, S.V.; D'Arpino, M. Critical Comparison of Li-Ion Aging Models for Second Life Battery Applications. *Energies* **2023**, *16*, 3023. <https://doi.org/10.3390/en16073023>

Academic Editors: Ahmad Hably, Reza Razi and Mehrdad Gholami

Received: 8 February 2023

Revised: 16 March 2023

Accepted: 18 March 2023

Published: 26 March 2023



Copyright: © 2023 by the authors. Licensee MDPI, Basel, Switzerland. This article is an open access article distributed under the terms and conditions of the Creative Commons Attribution (CC BY) license (<https://creativecommons.org/licenses/by/4.0/>).

Keywords: lithium-ion batteries; second life automotive batteries; aging models; DC fast charging; ancillary services

1. Introduction

The increased usage of battery energy storage systems (BESSs), predominantly lithium-ion battery batteries (LIBs), in electrified vehicles (EVs) is expected to lead to a large number of battery packs dismissed from vehicular applications once they reach the automotive end of life (EoL) [1,2]. Most automotive original equipment manufacturers (OEMs) define the EoL of the EV BESS as the time at which a 20% loss of capacity is measured [3–6]. Passenger EVs have an expected lifetime of 8–10 years, while for commercial vehicles this may be limited to be around 4–5 years [7]. The disposal of these battery packs after their automotive EoL has been a major concern, but it has also been noted that these battery packs still retain a considerable amount of energy and power capability, making them suitable for less demanding second-life applications, with the aim of extending the operational lifetime of automotive BESSs, reducing the environmental impact of battery waste, and providing a secondary revenue stream for EV owners [8]. Second life batteries (SLBs) can provide low-cost LIB-based BESS solutions for stationary grid-connected systems, enabling novel business models [9,10], while there is the possibility to harvest cell materials (or pack components) to build new cells (or battery systems). One of the most widely accepted solutions by OEMs and utility operators is to maintain the automotive format of the SLBs

after repair and refurbishment, and employ them in a second-life application or where energy/power density is not crucial (Figure 1) [11–15].

BESSs have the potential to improve grid reliability, power quality, efficiency, and flexibility; provide auxiliary services to the grid; support renewable energies; and delay system expansion/investments [16,17]. The integration of SLBs in grid-connected systems represents a great opportunity for cost reduction as well as performance improvement, concomitantly enabling the use of LIBs where it would otherwise not be economically viable [10,14,18,19]. However, several challenges need to be addressed in order to enable the wide-scale adoption of SLBs in power systems, such as the complexity of the control and energy management of large-scale SLB system architectures, the on-site estimation of the state of health (SoH), defining the accessible capacity, the heterogeneous degradation in the pack and the system, and the need for increasing reliability and diagnosability.

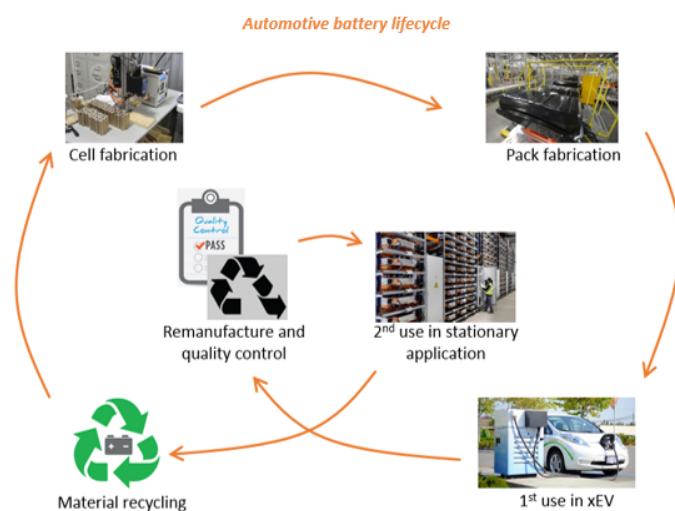


Figure 1. Life cycle of automotive battery packs.

The lifetime estimation and expected performance of a SLB system are very important aspects for the evaluation of the potential benefits of SLBs in their new application. They depend on the initial aging conditions at the beginning of their second life and the remaining useful life (RUL) and its evolution over time due to the new operating conditions. SoH and RUL prediction models are often used as metrics to define the appropriateness of the SLB; however, these parameters very rarely refer to a specific application or to the specific assessment methodology. Moreover, limited aging data are available for SLBs [11,20–22]; most of the prediction models have been developed for automotive applications and limited analyses have been performed to evaluate the performance of these models for SLB applications. Finally, several works in the literature have only considered the effect of SOH on capacity, while for several SLB applications, power fade becomes an important aspect concerning the reduced available power at low state of charge (SOC) values and the increased heat generation. Thus, an in-depth analysis considering how different estimation approaches may affect the lifetime analysis of SLBs is performed in this paper, taking both capacity and power fade into account.

The objective of this paper is to provide a comparative analysis between two different well-accepted model-based approaches for the estimation of the SoH and RUL considering several SLB applications. While there exist other SoH estimation approaches based on data-driven or purely physics-based models, these are not considered in this publication, since a widely accepted approach has not been identified by industry and academia for these SoH estimation methods. This research will help model users in understanding the strengths and weaknesses of different categories of degradation models and thus help them to select the most appropriate model for their specific SLB application. Comparative studies of different aging models used in hybrid electric vehicles are reported in [23–25]. The

authors in [23] report a comparison between empirical, semi-empirical, and physics-based aging models using common drive cycles. Ref. [24] focuses on diagnostic methods for battery aging estimation and carries out a qualitative comparison. Ref. [25] provides a detailed qualitative comparison between physics-based models, equivalent circuit models, machine learning models, and empirical and semi-empirical models for SoH estimation considering different chemistries. The comparative analyses available in the literature do not address calendar aging, power fade, and the specific challenges related to SLB application. Moreover, in many cases, the comparisons do not consider a common mission profile for a proper quantitative comparison between the different models. Finally, the dependence on the initial condition is very critical in SLB applications for the estimation of RUL and SoH; however, this has not been considered in the literature.

In this paper, a semi-empirical, physics-based [26,27] and empirical [28] aging model for LIBs have been selected as representative state-of-the-art methods for estimating the SoH and RUL, considering a number of citations and their applicability in SLB applications. These models have been calibrated in this work using the aging campaign data of LMO-MNC cells reported in [28]. These aging models are then coupled with an equivalent circuit model (ECM) of SLBs and a lumped parameter thermal model for the estimation of the capacity and the power fade experienced in SLB applications. The novelty of this paper includes:

- The consideration of calendar and cycling aging for both capacity and power fade.
- The comparison of different aging models calibrated using the same experimental data and the same test profiles.
- Different case studies, that are representative of typical grid-connected applications (such as bulk energy storage for peak shaving and frequency regulation for ancillary grid services), are considered.

The analysis included in this study intends to showcase the limitations and strengths of each aging model, as well as to provide insights into the applicability of the models to different usage scenarios. A quantitative comparison is provided.

The rest of the paper is organized as follows: Section 2 describes the two selected state-of-the-art battery degradation models; Section 3 analyzes the performance of the two models on the basis of the calibration and validation dataset; Section 4 defines developed case scenarios with different SLB applications and their key specifications; Section 5 reports the results and critical comparison of the two models when estimating the capacity and power fade for these applications; and finally, Section 6 concludes the paper with some key takeaways.

2. Battery Degradation Models

LIBs degrade due to time and usage conditions. At the cell output terminal, the degradation can be measured as capacity fade and power fade [25,29–31], and the change in these parameters over time is essentially referred to as ‘capacity fade’ and ‘power fade’ (SoH_C or SoH_R , as defined in [32]). A multitude of degradation mechanisms have been presented in the literature, the most accepted and well-understood processes are solid electrolyte interface (SEI) layer growth [25,33–36], the loss of active material in electrodes [25,37], gas generation [38], and Li plating [25,39]. These degradation processes affect LIBs through two modes, ‘calendar’ and ‘cycling’ aging. Calendar aging is primarily influenced by time and is accelerated by higher temperatures and higher storage state-of-charge (SoC) conditions. Cycling aging is caused by the usage conditions and is highly dependent on applied current, operating temperature, and depth of the discharge (DoD) cycles. Measurable/observable parameters (such as time, SoC, Temperature, DoD, current, etc.) often accelerate aging in LIBs and are referred to as ‘stress factors’.

The estimation of cell degradation as function of the stress factors is usually carried out with the help of model-based methods or data-driven methods [24,25,40–42]. Model-based methods have been widely used in the literature and a multitude of approaches are available, with differences in prediction fidelity, model complexity, computational

cost, and data required for calibration. In the literature, several classes of model-based battery degradation models have been proposed, such as physics-based models [27,34,43], semi-empirical models [7,26,44,45], and empirical models [28,46–49].

Empirical models are based on heuristic correlations between capacity/power fade and identified stress factor(s). The intensity of these correlations is usually modelled through severity factor expressions that are specific to each model approach and are calibrated using aging data [7,28,32,48–50]. A summary of the empirical models available in the literature is reported in [51]. These models are generally used for online SoH estimation employing simple model structures, while providing sufficient accuracy for most hybrid electric vehicle (HEV) applications [23]. Since the models stem from interpolating a large experimental dataset, they generally exhibit a validity limited to specific battery chemistry and operating conditions.

Physics-based models consider one or more aging phenomena modelled by considering physical relations; thus, they are typically computationally expensive and involve a higher number of calibration parameters. However, they are more robust than empirical approaches since they allow for accurately estimating physical behavior [33,35,39,52]. Additional complexity in these degradation models arises from the fact that some aging mechanisms are specific to the battery chemistry and the inter-coupling of the different aging mechanisms.

Semi-empirical models can either be model-order reduced physics-based models [26,45] or based on salient mechanisms determined by aging experiments [7,44]. By eliminating the inherent computational complexity associated with partial differential equations for Li ion transport, as seen in complex electrochemical aging models, semi-empirical reduced-order models significantly conserve computational resources.

In this paper, two model-based aging models (a semi-empirical physics-based model and an empirical model) are selected based on their completeness, calibration effort, and popularity in the literature and will be described in the following sections.

2.1. Empirical Model

The model proposed in [28] is considered in this work as one of the most accepted and complete in the literature. This model includes both calendar and cycling aging for capacity and power fade and considers the most important stress factors. Moreover, the model has been calibrated and validated for several LIB chemistries over a wide range of experimental data. This model will be henceforth referred to as EM.

The EM is based on Dakin's equation of degradation, where the cell capacity (Q) and internal resistance (R) are described by the following relation:

$$\frac{d\zeta}{dt^\alpha} = \pm k_{tot} \cdot \zeta^n \quad (1)$$

where ζ represents Q or R at the current instant t , α is a time-dependent factor, and n is the order of the reaction (equal to one for the chemistry considered in this study). The positive and negative signs take into account the internal resistance rise and capacity decrease, respectively. k_{tot} is the total degradation rate and can be expressed as the product of the calendar and cycling degradation rate, k_{cal} and k_{cyc} , respectively:

$$k_{tot} = k_{cal} \cdot k_{cyc} \quad (2)$$

where

$$k_{cal} = \frac{1}{\Delta SoC} \int_{SoC_{min}}^{SoC_{max}} \exp\left(\frac{c \cdot SoC}{a}\right) \cdot \exp\left(\frac{d}{a}\right) \cdot \exp\left(\frac{-b}{aT}\right) \cdot dSoC \quad (3)$$

$$\ln(k_{cyc}) = \exp\left(\frac{a_3}{RT} + b_3\right) \cdot \frac{I}{I_0} \quad (4)$$

k_{cal} is a function of SoC and temperature, T , and captures the calendar aging phenomena; however, ΔSoC and the SoC integral are included to evaluate the degradation due to the SoC cycle. k_{cyc} is then a function of the applied current I (in Amps) and T . The calibration of this model requires a variety of parameters, such as $n, \alpha, a, a3, b, b3, c, d$, and I_0 , for both capacity and power fade.

2.2. Semi-Empirical Physics-Based Model

The semi-empirical physics-based model considered in this work is described in [26,45] and, in this work, has been augmented with the power fade model reported in [27,53]. Thus, the combined model includes both capacity and power fade mechanisms due to calendar and cycling aging. This model will be henceforth referred to as PBM. The model structure is reported in Figure 2 and captures the aging mechanisms that can happen to the cell anode, such as SEI layer growth with diffusion kinetics and structural changes in the active material (LAM) caused by mechanical stresses during cycling. The PBM was obtained by reducing physics-based models and introducing empirical parameters.

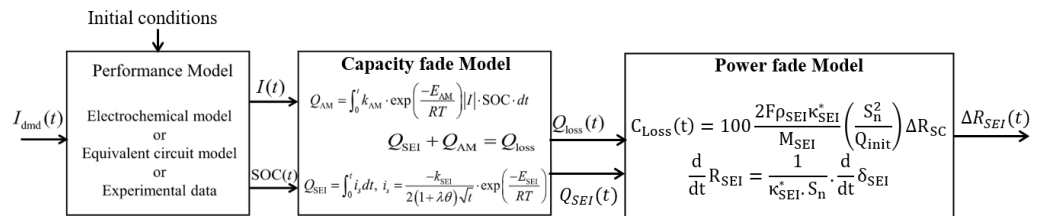


Figure 2. Structure of the physics-based model.

The total capacity loss is estimated as the sum of the capacity losses contributed by the SEI layer growth (Q_{SEI}) and the LAM (Q_{AM}). The SEI layer growth manifests itself as the loss of cyclable lithium in the LIB (Equation (5)) and an increase in film resistance (Equation (9)) to the lithium transport to/from the electrode surface. It is here modelled using a mixed kinetics–diffusion limited approach at the graphite/SEI interface [26].

$$Q_{SEI} = \int_0^t -\frac{k_{SEI} \exp\left(-\frac{E_{SEI}}{RT}\right)}{2\sqrt{t}(1 + \lambda \cdot \theta)} dt \tag{5}$$

The capacity loss due to SEI growth is influenced by the side reaction current density and is aggravated by higher operating temperatures (T) and the variation in overpotential (θ). The dependence of capacity loss on LAM is highlighted by the reduction in the active material volume fraction of the anode and the increase in current density [45], and is influenced by cycling-induced intercalation/de-intercalation processes.

$$Q_{AM} = \int_0^t k_{AM} \cdot \exp\left(\frac{-E_{AM}}{RT}\right) \cdot SoC \cdot |j_n(t)| \tag{6}$$

Then, the total capacity fade can be calculated as follow:

$$Q = Q_{SEI} + Q_{AM} \tag{7}$$

The calibration of the capacity loss estimation in the PBM involves fitting pseudo-physical parameters, such as $k_{SEI}, E_{SEI}, \lambda, k_{AM},$ and E_{AM} (Figure 2). Moreover, it requires solving a partial anode-side electrochemical model (such as the extended single particle model [52]) to estimate the kinetic overpotential and the open circuit potential of the anode and thus the overpotential of the side reaction (Equation (4) in [26]).

This paper augments the aging model proposed in [26,45] by including the power fade model proposed in [27,53]. This model accounts for the impedance rise caused by the SEI layer with aging (R_{SEI}) using the ionic conductivity, κ_{SEI}^* , as shown in Figure 2. The other contributions of the impedance rise such as charge transfer and electrolytic ohmic re-

sistance (Equation (8)) are ignored in this paper, since their evolution with aging is not well understood. The cell internal resistance can be modelled by the following contributions:

$$R_{total} = R_{ohmic} + R_{ct,n} + R_{ct,p} + R_{SEI} \quad (8)$$

The R_{SEI} is then modelled as the following:

$$\begin{aligned} \frac{dR_{SEI}}{dt} &= \frac{1}{\kappa_{SEI}^* \cdot S_n} \frac{d\delta_{SEI}}{dt} \\ \frac{d\delta_{SEI}}{dt} &= -\frac{i_s \cdot M_{SEI}}{2F \cdot \rho_{SEI}} \end{aligned} \quad (9)$$

where the SEI layer thickness, δ_{SEI} , is calculated by the capacity fade model, Equation (5). The values of M_{SEI} , κ_{SEI}^* , and ρ_{SEI} are tuned with calendar conditions (Figure 3). It is important to point out that the evolution of power fade does not follow a linear relation with the capacity fade, as reported in [27] for LFP chemistry. In fact, R_{SEI} accounts for both SEI layer growth in increasing the loss of lithium inventory (LLI) and SEI film resistivity. Equation (10) attributes capacity fade to its driving phenomena: loss due to SEI growth and AM loss (affecting S_n).

$$\kappa_{SEI}^* = \frac{Q_{loss,\%} \cdot Q_{nom} \cdot M_{SEI}}{\Delta R_{SC} \cdot 2F \rho_{SEI} \cdot S_n^2} \quad (10)$$

CALENDAR AGING				CYCLING AGING				
Fixed T°C	30°C	45°C	60°C	Average 60% SoC	Mean T°C	40°C	45°C	50°C
Fixed SoC(%)					ΔDoD(%)			
30%	PBM C	PBM C	PBM V		Δ20%	③ PBM C		① PBM C
	EM C	EM C	EM C			EM C		EM C
65%	PBM C	PBM C	PBM C		Δ20%			② PBM V
	EM C	EM C	EM C					EM C
100%	PBM V	PBM V	PBM V		Δ30%		⑤ PBM V	
	EM C	EM C	EM C				EM V	
					Δ40%	④ PBM V		
						EM C		

Figure 3. LMO-NMC dataset and how it is used for calibration and validation of EM and PBM. ‘C’ and ‘V’ represent the conditions used for calibration and validation, respectively. The numbers in the circle indicate the different power profiles used during the aging campaign.

3. Aging Models Calibration and Validation

By comparing the EM and PBM aging models, various inferences can be derived from model structures, calibration procedures, and the ability to capture different aging conditions, which can aid in assessing the capabilities and their applicability in various SLB applications (Section 5). Experimental data from an aging campaign are usually used to calibrate and validate an aging model under different operating conditions. The aging campaign can be properly sized depending on the model capability of predicting physical correlations.

An LMO-NMC/graphite battery chemistry is considered for this analysis due to the completeness of aging data available in the literature, reported by the SIMSTOCK/SIMCAL project in [28,46,54–56] on the 5.3 Ah LG Chem cell and data reported by [47] on the 15 Ah LG Chem cell. These extensive aging campaigns report a rich dataset for capacity and power fade at different temperatures (10 °C, 30 °C, 40 °C, 45 °C, 50 °C, and 60 °C), SoC conditions (30, 65, and 100%), current levels (5C, 10C, and 20C), and cycling profiles, showing the effects of calendar aging over a 3-year timescale and cycling aging over a few thousand Ah throughput.

Figure 3 shows how the available data have been used for calibrating and validating the two aging models considered in this study.

It is noted that the EM requires an extensive set of conditions to accurately fit capacity and power fade trends [28], while the PBM requires only a specific set of operating

conditions to calibrate the necessary model parameters [26,45]. Thus, the validation of the EM can be performed within the boundary conditions of the calibration range, while the PBM may allow for some extrapolation. Although the EM and PBM utilize the same experimental data, the calibration procedure and the required tools are very different. The EM is calibrated by curve fitting the model structure to the experimental aging data to identify model parameters for both capacity and power fade over several operating conditions; the accuracy of EM is often related to the amount of data available to be fit and the dependency of the calibration parameters on the operating conditions. On the other hand, the PBM requires a more complex procedure involving an electrochemical model for the prediction of the anode overpotential to physically correlate the semi-empirical parameters to the aging trends observed in the reported dataset. The electrochemical model used in this work and the related calibration procedure are outlined in Appendix A. The SEI growth parameters, Equation (5) are calibrated using only five out of nine calendar aging conditions, as seen in Figure 3, and the rest are used for the purpose of validation. In cycling aging conditions, the Q_{SEI} is estimated using the current profile shown in the SIMSTOCK project [28] and Equation (5) along with the calibrated SEI growth model parameters. Q_{AM} is further calculated in cycling aging by subtracting the cycling Q_{SEI} from the experimental data for capacity loss, Equation (7)). The calibration of the Q_{AM} parameters is achieved by fitting the parameters of (6) with this subtracted capacity loss and stress factors, such as current density, SoC , and temperature. The calibration of the power fade model involves the calibration of κ_{SEI}^* for this cell using the correlation reported between capacity fade and power fade in Equation (10). Parameters such as δ_{SEI} and S_n are obtained from the capacity fade model, since the physical losses in the cell have a simultaneous effect on capacity and power fade. As pointed out in Section 2, the κ_{SEI}^* parameter is tuned using the data obtained using conditions of $T = 30^\circ C$ and $SoC = 30\%$ from Figure 3, with the assumption that the capacity fade under these conditions is driven purely by SEI growth, without the interference of additional degradation mechanisms. It is also assumed that the electroactive surface area, S_n , is constant in calendar aging since there is no active material loss. The calibrated value of κ_{SEI}^* is used along with the molar mass and density as the SEI layer parameters from [27] in Equation (9). Once the parameters are calibrated for the PBM, the inputs to the aging model can be obtained from an equivalent circuit model or experimental data, depending upon availability.

In summary, the EM is calibrated using the whole dataset to allow for better accuracy, while the PBM utilizes specific operating conditions to excite different aging mechanisms and thereby calibrate the related parameters. The EM calibration requires a large dataset of operating conditions, whereas the PBM requires limited operating conditions to capture the physical aging phenomena.

The calibrated parameters for the EM capacity and power fade are reported in Table 1, while Table 2 reports the parameters for the PBM.

In following figures, the acronym 'T X SoC Y' identifies the calendar data collected for a cell stored at a temperature of X and an SoC of Y, while the cycling conditions are identified by the profile number shown in Figure 3.

Table 1. Empirical model: calibrated capacity fade and power fade model parameters.

Calibration Parameters	α	a	b	c	d	a3	b3
Units		$Jmol^{-1} K^{-1}$	$Jmol^{-1}$	$Jmol^{-1} K^{-1}$	$Jmol^{-1} K^{-1}$	$Jmol^{-1}$	-
EM Capacity Fade	1	8.314	67,801	34.2	131.3	49,450	-24.06
EM Power Fade	1	8.314	57,816	29.2	111.24	49,450	-24.06

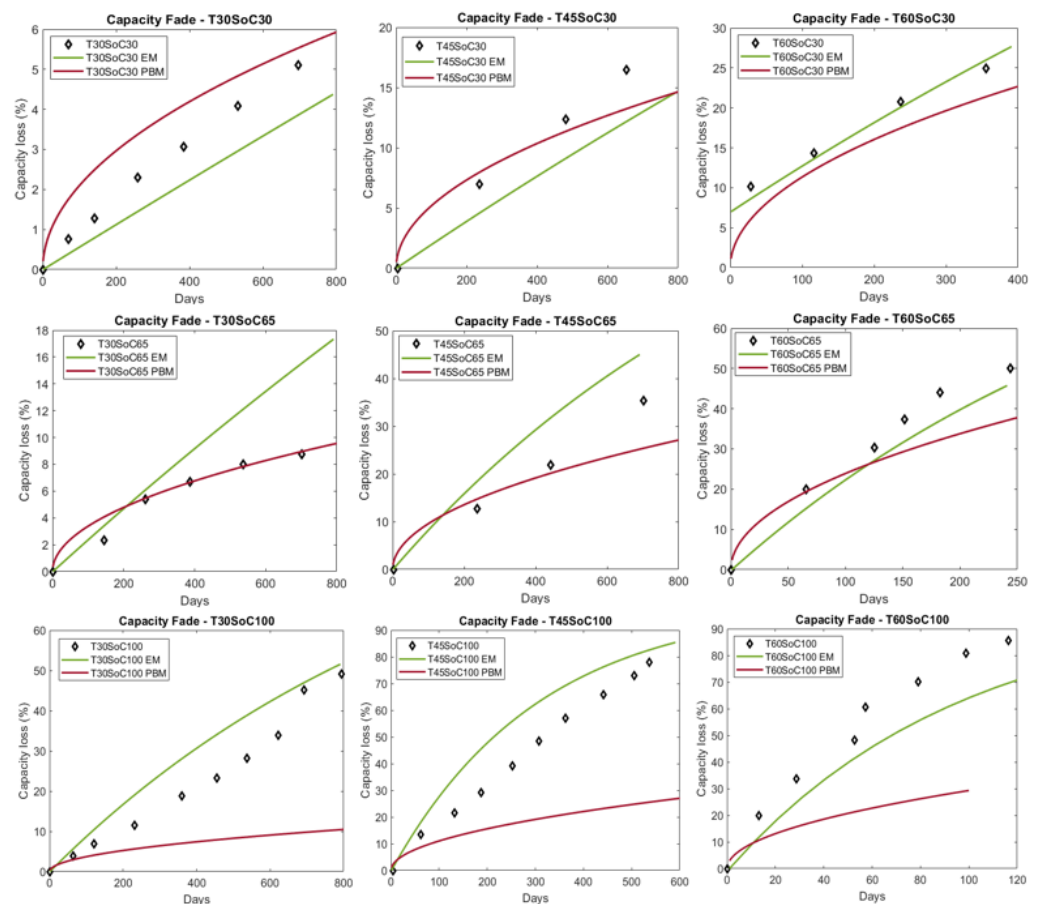
Table 2. Physics-based semi-empirical model: calibrated capacity and power fade model parameters.

	E_{SEI}	k_{SEI}	λ	E_{AM}	k_{AM}	κ_{SEI}^*
Units	Jmol^{-1}	$\text{s}^{-1/2}$	-	Jmol^{-1}	Ah^{-1}	Sm^{-1}
Calibration set (PBM)	5.419×10^4	6783.7	1.4149×10^6	5.4193×10^4	632.62	2.17×10^{-7}

3.1. Capacity Fade

Figure 4 show a comparison between the experimental data and the EM and PBM results in calendar aging conditions. Table 3 reports the absolute error of the capacity fade estimation at the end of the aging campaign.

The structure of these aging models are reliant on time as a stress factor, albeit in different configurations. From Equation (1), the relationship between ‘ ζ ’ and time is a double exponential relationship, which is reduced to a single exponential since the ‘ α ’ term is assumed to be unity, similar to [28]. The formulation of the model structure for the EM is strictly correlated with the acquired experimental data and predefined dependence on specific stress factors.

**Figure 4.** Comparison of capacity fade in calendar aging between aging data for the EM and PBM.

It is worth noting that both models fail under specific operating conditions. The PBM fails to accurately predict the capacity fade at a high SoC and high temperatures. This is likely attributed to the fact that the PBM does not include aging mechanisms that may occur under these conditions, such as transition metal dissolution. As matter of fact, the PBM does not account for all aging mechanisms occurring at these high stress factor conditions [26,45]. At higher SoC conditions (high positive electrode potentials > 4.3 V) in Mn-rich cathodes, Mn^{2+} ion dissolution from the cathode becomes evident [57]. It is

also reported in [57] that a rapid SEI growth may ensue from this Mn ion transport, and is aggravated by higher temperatures that are favorable for SEI growth.

Table 3. Mean absolute error for capacity fade in calendar aging with all models (expressed in %).

Calendar Scenario	EM	PBM
T30SoC30	0.176	1.771
T30SoC65	4.713	2.107
T30SoC100	11.52	14.157
T45SoC30	2.503	1.594
T45SoC65	5.275	3.772
T45SoC100	10.160	25.992
T60SoC30	1.005	2.979
T60SoC65	6.104	8.035
T60SoC100	6.680	21.426

The performance of the EM prediction in calendar aging is dependent on the magnitude of the severity factors in the model structure. The rate of aging in the EM is determined by an exponential function and thus a low severity factor magnitude (SoC \leq 65% and $T \leq 45$ °C) tends to yield a linear aging rate with time compared to a high severity factor magnitude that yields an exponential rise in the aging rate, as seen in Figure 5. Since the EM is calibrated by regression over the entire set of aging conditions, the overprediction of some conditions occurs in low severity factor conditions, while the PBM performs better in estimating these conditions. The shape of the degradation prediction with time is seen from the capacity loss due to the SEI growth equation (Figure 2), through a \sqrt{time} relationship.

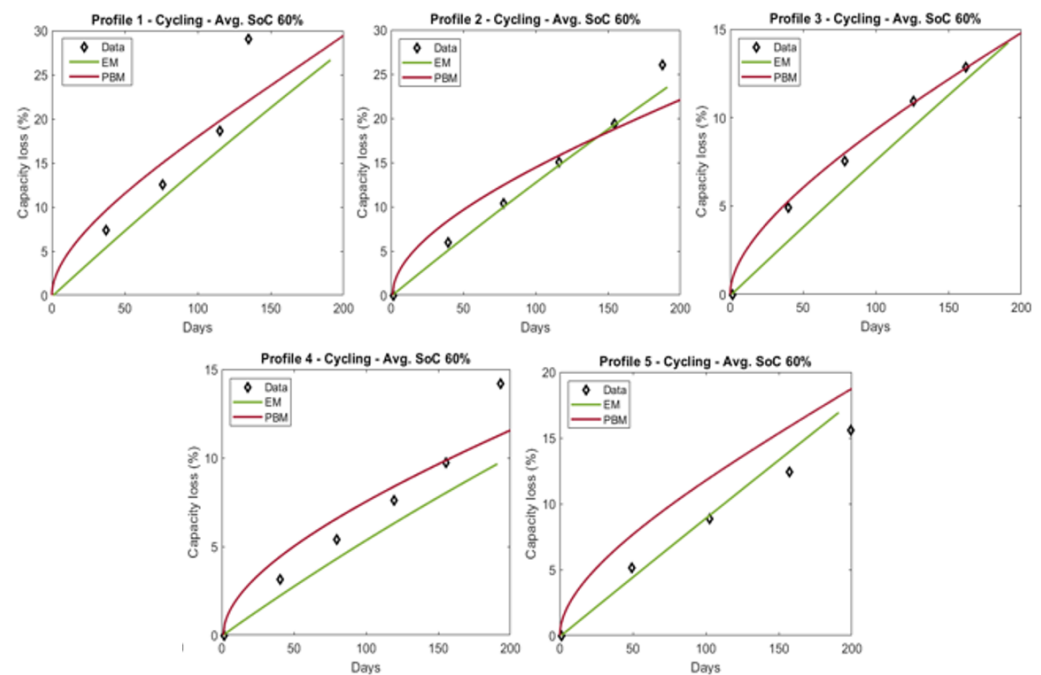


Figure 5. Comparison of capacity fade in cycling aging between aging data for the EM and PBM. The cycling conditions are identified by the profile number in Figure 3.

Using the five current profiles reported in the SIMSTOCK project [28], the EM and PBM are used to evaluate their response to cycling and calendar aging conditions. In the case of cycling aging conditions, the performances of the EM and the PBM are comparable in all conditions, within 3% mean absolute error. Figure 5 and Table 4 report the comparison of the experimental data with the EM and PBM calibration. The trend seen in the EM is mostly linear for all conditions, because the severity factors associated with the SoC and temperature are not high. However, it is expected that the curve of the PBM will start to saturate given the reduction in the SEI layer growth rate, whereas the EM is expected to outpace this loss with overprediction due to the model structure.

Table 4. Mean absolute error for capacity fade in cycling aging with all models (expressed in %).

Cycling Scenario	EM	PBM
Profile 1	3.06	2.57
Profile 2	0.79	1.89
Profile 3	1.12	0.38
Profile 4	3.20	1.13
Profile 5	0.66	2.61

3.2. Power Fade

Figure 6 and Table 5 show the results of the calibration of the power fade in calendar aging conditions, while Figure 7 reports the same results under cycling aging conditions. The trends in the prediction of a rise in resistance from the PBM in calendar aging conditions are similar to the capacity fade prediction (Figure 6). The reason attributed to this is that the power fade model using the PBM only takes into account the resistivity of the SEI layer growth, which is dependent on the thickness of the SEI layer. Again, it has been observed that the higher SoC and temperature conditions were not captured accurately by the PBM, incurring a high prediction error. The EM has a better fit across all aging conditions, given that it is regression-based, and also shows exponential curvature when severity factors are higher (Figure 5). The power fade in cycling data was not reported in [28] and thus, the calibration sets for the PBM and EM in calendar aging were extended to estimate the power fade. The prediction given by the EM and PBM are comparable for most conditions, showing similar trends to the capacity fade in cycling conditions, as seen in Figure 7.

Table 5. Mean absolute error for the resistance increase in calendar aging with all models (expressed in %).

Calendar Scenario	EM	PBM
T30SoC30	7.955	4.505
T30SoC65	6.467	6.57
T30SoC100	18.83	82.16
T45SoC30	25.644	12.736
T45SoC65	17.429	25.046
T45SoC100	162.80	101.532
T60SoC30	9.357	52.616
T60SoC65	96.375	89.480
T60SoC100	120.74	97.193

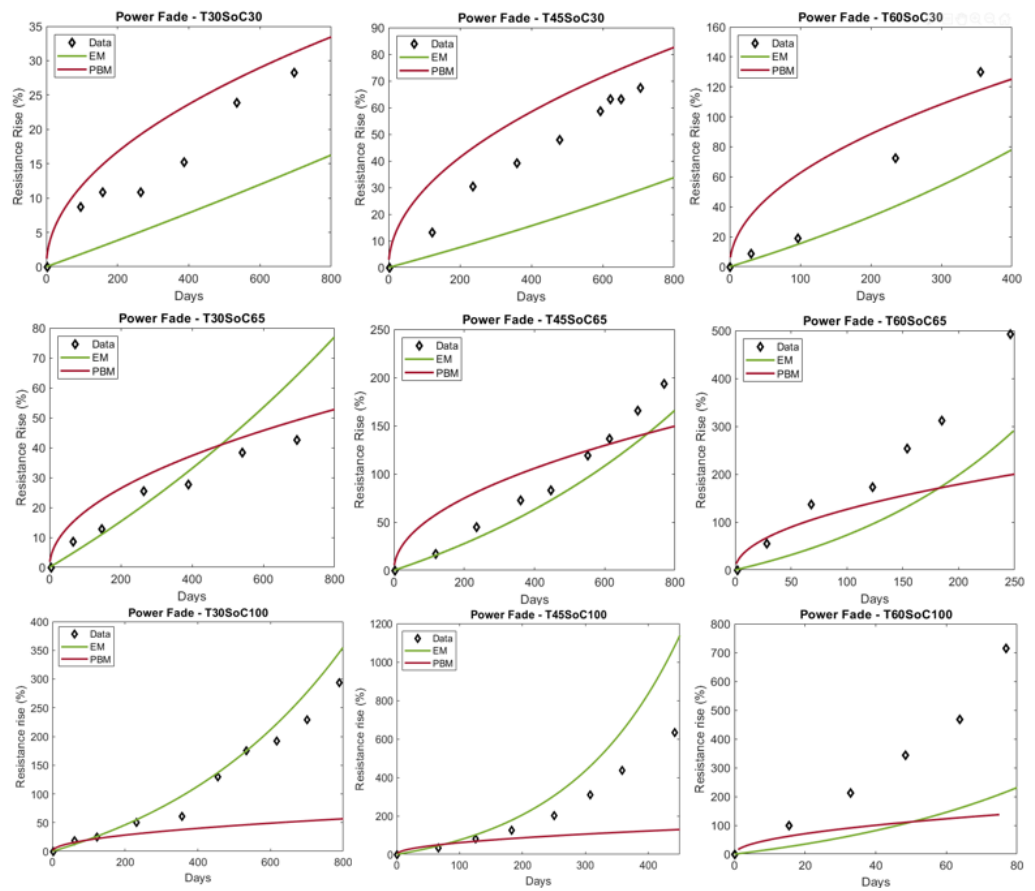


Figure 6. Comparison of resistance increase in calendar aging between aging data for the EM and PBM.

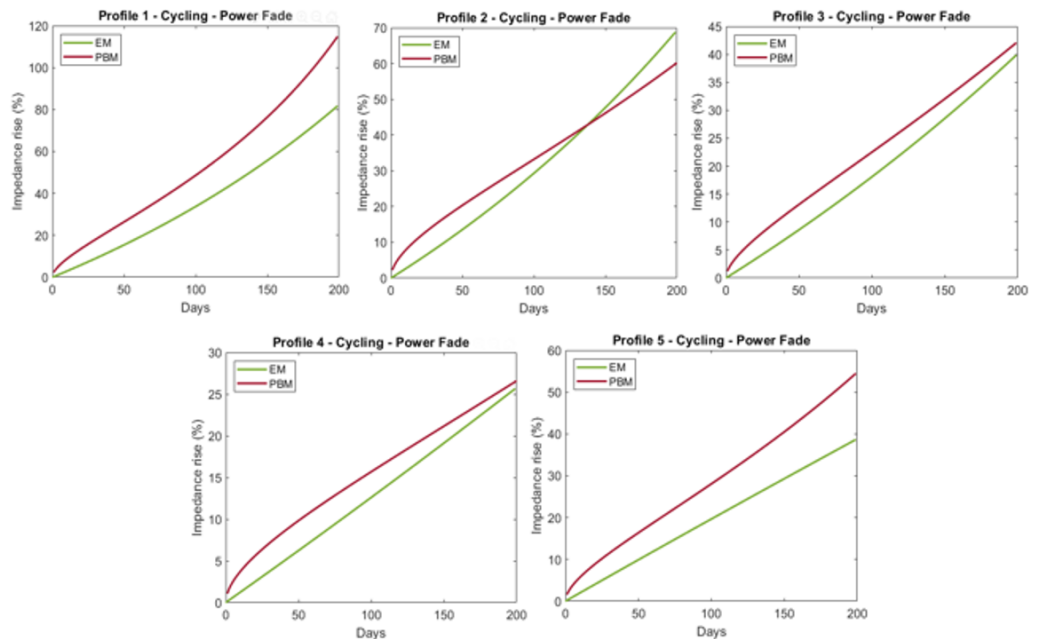


Figure 7. Comparison of resistance increase in cycling aging between EM and PBM. The cycling conditions are identified by the profile number in Figure 3.

4. SLB Profile Definition and System Design

This paper considers various SLB applications for retired traction battery packs catering to the LV power grid level. Two classes of SLB applications are considered in this work

and three profiles have been defined, the representative power demands are shown in Figure 8 [58] and described below:

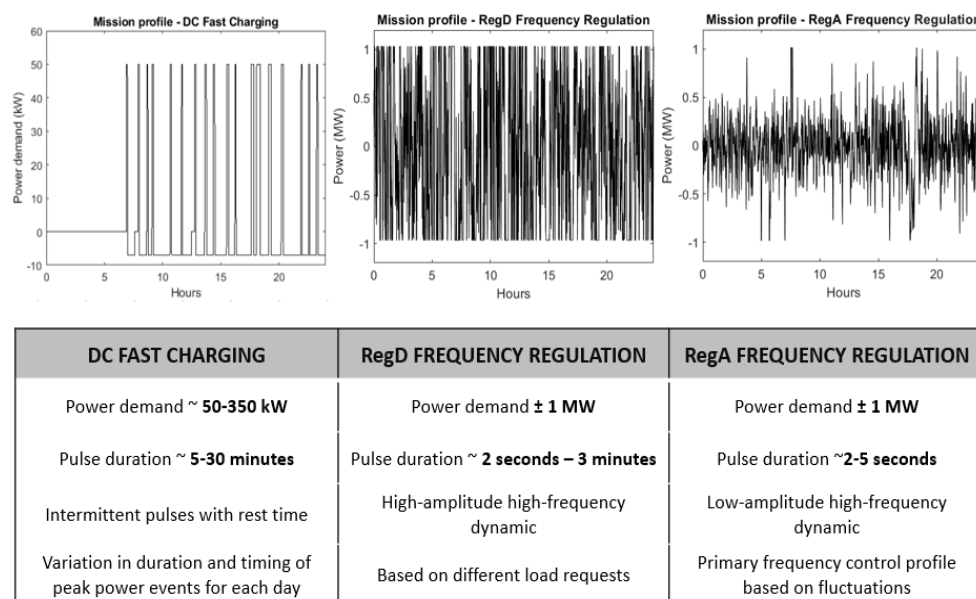


Figure 8. Second-life application power demand profiles.

1. Peak shaving (DC fast charging—DCFC): this concept has been investigated in detail in [11,19,31,58–60], focusing on reducing the burden imposed by high peak power demands from the DC fast charging stations on the grid by utilizing SLBs as buffers between the charging station and the grid.
2. Ancillary services (Frequency regulation—FR): BESSs offer a rapid response and an emission-free operation compared to traditional generators, responding to the increase or decrease in grid frequency and maintaining the optimal frequency [58]. Participants for frequency regulation may be required to satisfy either or both of the regulation signals as certified by the regional transmission operator (RTO), specifically PJM in this paper.
 - RegA signal: slow moving signal similar to traditional regulation services such as generators, etc.
 - RegD signal: fast moving signal and the performance compensation given to participants is higher for RegD signals compared to RegA due to the higher mileage ratio.

Additional information on the mileage and compensation are outlined in PJM Manual, Volumes 12 and 28.

The pulse duration from Figure 8 for DCFC can be between 5 and 30 min and is based on EV charging events throughout a typical day. While the DCFC profile is measured in the kW range, the FR profiles are studied in the MW range, since it caters to the level of the local distribution grid. The ancillary services provided to the grid require a rapid response as well as the capability to operate at maximum/minimum power limits for a sufficient amount of time. The RMS value of the RegA mission profile is less than 25% of the peak value, implying that the RegA profile generally operates at low power. This profile varies on the time scale of seconds, implying an application in primary frequency regulation [61]. The higher compensation provided for the RegD signal corresponds to faster transients and the most common high power operation, which corresponds to the need for a higher number of batteries to satisfy the energy demand profile.

4.1. Simulator Architecture

A comparison of the PBM and EM was carried out with the simulator shown in Figure 9. The simulator framework includes a second-life power demand profile input between the three case studies, considering an initial size estimate, and is discretized in seconds for both aging models for all mission profiles to capture the required accuracy. An electro-thermal SLB pack model takes the input from the sizing analysis and runs a real-time simulation using a zeroth-order equivalent circuit model and a lumped parameter thermal model calibrated using a 23-kW 2012 Ford Focus EV battery pack with LMO-NMC chemistry pouch cells [31]. The parameters of the battery pack are reported in Table 6. The simulator uses a similar electrical and thermal performance model to the one implemented in [11,31,58,60].

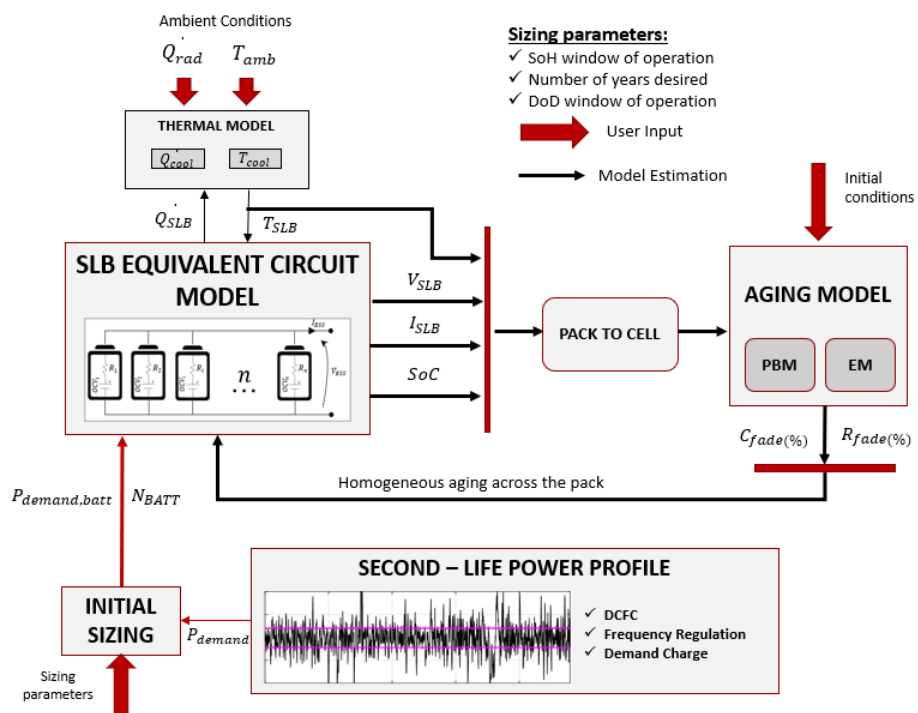


Figure 9. Second-life model comparison simulator framework with battery performance and thermal models at the pack scale and the aging models at the cell scale.

Table 6. Battery parameters at SoH = 100%.

SLB nominal capacity	73.5 Ah
SLB usable capacity	59 Ah
SLB resistance at SoC = 50% capacity	0.1 Ω
SLB SoC operating range	(15, 95)%
SLB voltage range	260–360 V
SLB max power in disch/charge	110 kW, 60 kW
SLB temperature	(−10, 45) °C

The inputs for the two aging models, such as temperature, current input, and SoC, are obtained from the electro-thermal model of the SLBs. The downscaling of current from pack level to cell level assumes uniform aging and current distribution across all cells, which means the resistance of each parallel string of cells is the same and thus the current is evenly split between the cells. This assumption is key, since the real-time cell internal resistance/current split between parallel strings cannot be implemented, unless with an online BMS on a physical pack.

The entire simulator was implemented in Matlab software with user inputs on SLB application and desired simulation parameters such as SLB parameters, the SoH window

of analysis, ambient temperature dynamic, etc. The PBM was implemented in Simulink and ran in real-time with the simulator, with an ODE4 Runge–Kutta fixed-step solver and time step of 1 s, since it is solved over hundreds of days. The simulator can be extended for different cell/pack configurations and can also account for different chemistries if the aging models are accurately calibrated for the specific chemistry. Since the discretization is in seconds for both the semi-empirical physics-based model and the empirical model, we cannot clearly distinguish between the simulation times of both models.

4.2. System Design

Considering the three power profiles defined in Figure 8, the SLB system needs to be sized accordingly to fulfill the mission profiles and meet the sufficient performance and lifetime requirements. Oversizing the SLB system will increase the initial investment costs and system complexity, but conversely, cycling aging is usually reduced, while calendar aging will heavily depend on the SoC at which the batteries are resting. The undersizing of the system will usually result in more replacements of SLBs, as shown in [11], and may fail to satisfy the mission profile requirements. Thus, to perform a proper comparison between the different aging models and consider different mission profiles, choosing an appropriate size of the SLB system is required.

In this paper, the sizing procedure involves an iterative approach with the aim of defining the critical number of batteries that can satisfy the power profile demanded by the application while staying within the prescribed SoC and temperature limits of the battery technology. Figure 10 shows the critical limit of the batteries for each power profile considering an initial SoH of 90%. The SoH is initialized as a numerical correction of the pre-exponential factor for the EM (Equation (1)), whereas the PBM necessitates a first-life simulation to accurately identify the initial conditions of SEI growth, AM loss, and Ah-throughput for second-life aging estimations. The chosen initial conditions for the PBM are obtained after simulating a 10% capacity loss using a pseudo electric vehicle usage profile. The SoH window was restricted to simulate second-life applications from 90% to 70% residual capacity, keeping in mind the limited availability of validation data in this region of capacity loss. The power profile in the simulation is also required to have a net zero energy throughput each day, i.e., the initial SoC and final SoC for each day remain the same. This is imposed so that the SoC drift with time can be exclusively attributed to aging alone. It is crucial to understand that the system sizing is conserved and only carried out at the initial SoH of the SLBs. It is also assumed that the representative power profiles are repeated everyday.

Figure 10 also shows some of the parameters of the SLB design for the different mission profiles. In detail, the proposed grid-connected mission profiles have different average SoCs and temperatures to ensure a proper comparison of the EM and PSB over a wide range of operating conditions.

Profiles	Critical Limit of batteries	SoH window (%)	SoC window (%)	Average SoC (%)	Range of heat generation (kW)		Average heat generation (kW)	Average battery temperature (°C)	Max. C-rate (-)
DCFC	3			85	0	0.29	0.03	30	0.5 C
RegD	51	90% to 70%	95% to 10%	57	0	0.44	0.1505	21	0.9 C
RegA	19			44	0	2.49	0.1540	25	2.2 C

Figure 10. SLB system design and thermal parameters.

The effect of these power profiles at the pack level are of more interest than at the system level, since the aging models are calibrated on the individual cell scale. The number of batteries satisfying each mission profile dictates the applied current to each pack, thereby influencing the amount of heat generation, cell SoC, and the C-Rate, as shown in Figures 11 and 12.

The heat generation at the pack level is highest for the RegA profile, closely followed by the RegD profile, as shown in Figure 11. The heat generation for these profiles is comparable since their power demands are on the MW scale, while the kW scale of the DCFC profile, along with the lower number of batteries, contributes to a lower heat generation. Although the RegD profile is more demanding in terms of power requirements, the higher value of the critical number of batteries chosen causes the average heat generation to be lower and comparable to FR. Note that the heat generation in this work includes reversible and irreversible generation.

Figure 12 shows the C-Rate and SoC distributions on the pack level for the three different mission profiles at day 1 and day 100 of operation, showing the evolution over time. It is noted that the C-rate and the DoD increase with time due to the reduced capacity of the pack and resistance increase.

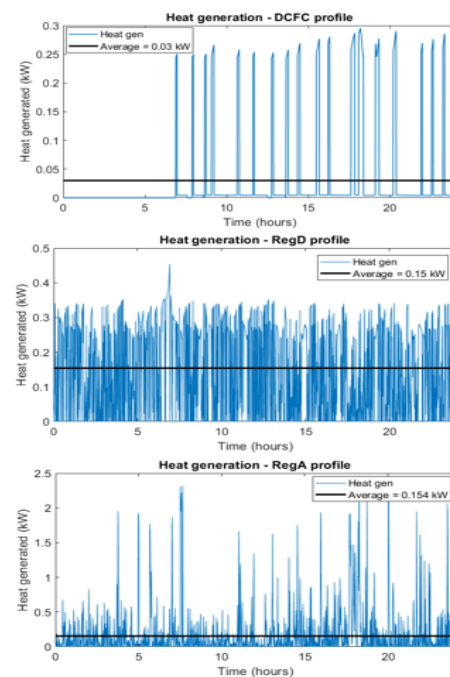


Figure 11. Heat generation on the pack level with power profile normalized by the critical number of batteries for each application.

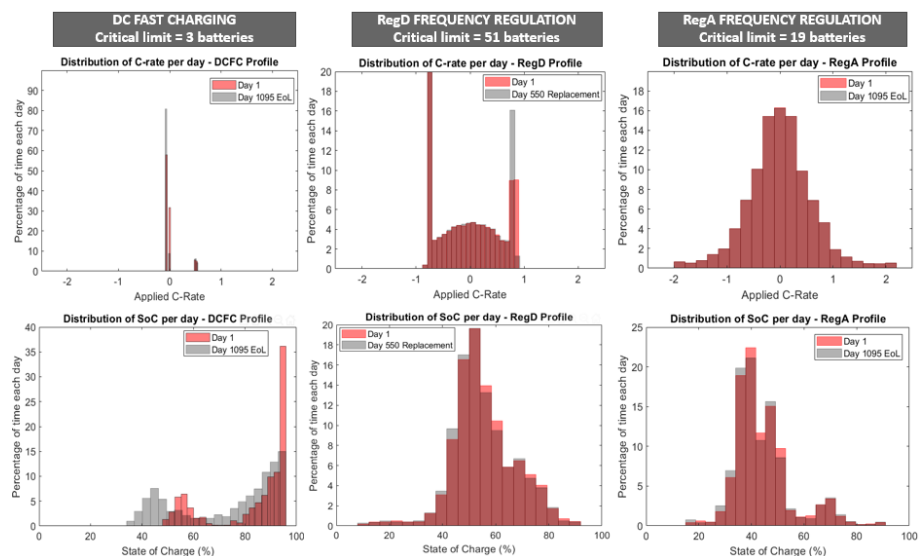


Figure 12. C-rate and SoC distributions on the pack level with power profile normalized by the critical number of batteries for each application.

5. Validation of Two Aging Models for All Profiles

In this section, the EM and PBM are used to evaluate the capacity and power fade of the SLB system sized for the three different applications in Section 4 over 3 years of operation. The initial SoH of the SLB is set to 90%. The model described in Section 4 is used for this analysis.

5.1. DC Fast Charging

In this application, the battery packs are required to stay at a higher SoC for the majority of the time to act as an energy buffer and be readily available to provide power to EVs during the charging event. Storing BESSs at a high storage SoC (stress factor) is the key aspect of this DCFC power profile, which aggravates aging. At the pack level, the current demands during both charging and discharging are minimal and intermittent, and the predominant aging effect is deemed to be calendar aging.

The capacity and power fade predictions by the EM and PBM for the DCFC profile are shown in Figure 13a. It is noted that battery pack replacement is not required in this application and that the degradation phenomena are impacted by the ambient temperature variation, exhibited by an oscillating capacity and power fade. The experimental data from the calendar aging conditions of $T = 30\text{ }^{\circ}\text{C}$ and $\text{SoC} = 100\%$ are overlaid for reference, and represent the closest conditions to SLB operation in this application, as shown in Figure 10. It is observed that the PBM severely underpredicts the capacity and power fade compared to the EM. This is in accordance with the results we observed in Figure 4, where the PBM fails to capture calendar degradation phenomena at high SoC conditions due to the transition metal dissolution phenomenon. The EM better predicts the SLB degradation compared to the reference conditions since the calibration is performed over a broad range of SoC and temperature conditions. The EM predicts a capacity degradation rate of 13% per year, with the dominating capacity loss due to SEI growth. Since the physics-based power fade model does not have sufficient validation data, we have chosen to take the empirical correlations for power fade to estimate the current profile for each day, and applied this to both models.

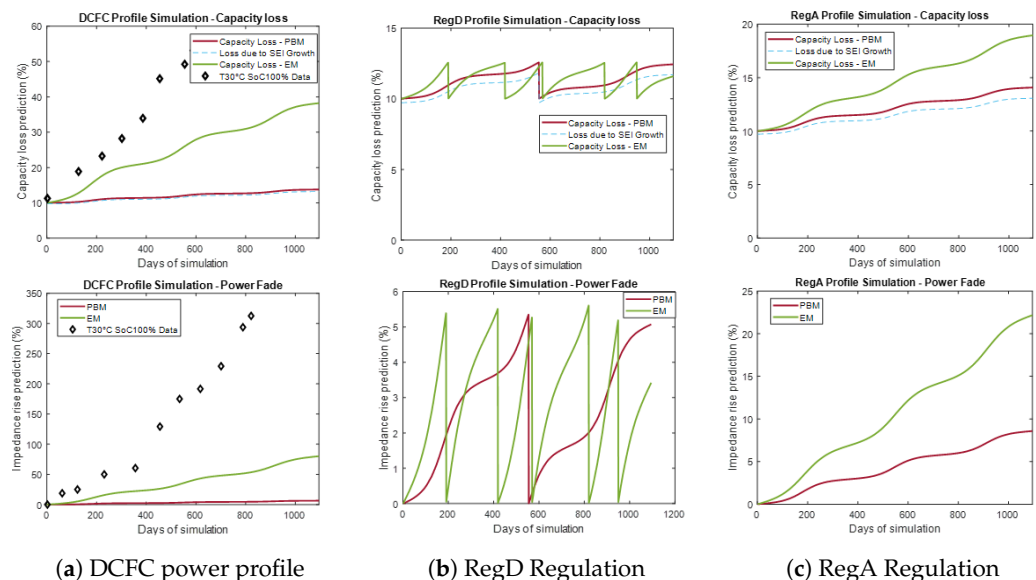


Figure 13. Comparison of capacity and power fade prediction of the EM and PSM for three different power profiles.

5.2. RegD Frequency Regulation

The characteristics of the RegD profile have previously been explored in detail in the above sections, refer to Figure 8. Under these operating conditions, the battery packs are

subjected to continuous current demands and operation at maximum/minimum power limits to satisfy the mission profile.

As shown in Figure 13b, when the battery pack can no longer be maintained within the SoC limits of operation, it fails to satisfy the mission profile and mandates a replacement of the SLB packs. Every replacement event will bring the battery to an initial state of SoH = 90%. The replacement rate is key to understanding the economic value, as it outlines the durability of the system for that mission profile. A comparison of capacity and power fade predictions given by the EM and PBM are shown in Figure 13b. Furthermore, in this case, the ambient temperature variation affects the dynamics of the SLB degradation. The figure also reports the estimated aging component related to SEI growth for the PBM. The difference between the PBM estimation and the one related to SEI growth is due to LAM and driven by cycling operation. The provided results also demonstrate the dominance of calendar aging in this operating condition. It is observed that the LAM loss is slightly higher in the RegD case, but is still lower than the capacity loss attributed to SEI growth. This is because of the higher capacity loss due to SEI growth observed in the battery's first life, which influences the trajectory of the PBM in its second life. The capacity degradation rate for this profile is close to 1% per year, with the capacity loss due to LAM accounting for nearly 25% of the total degradation rate. The EM on the other hand is mostly on the linear portion of the exponential curve, since the severity factors in the model structure are not high enough at this average temperature, current, and SoC value, as shown in Figure 10.

The replacement dictated by the PBM is due to a resistance rise of around 17% at 900 days, whereas the replacement dictated by the EM at different intervals is triggered by the capacity loss, pushing the SoC to below its lower limit. Thus, this capacity loss value is deemed critical for the RegD application and chosen sizing design. Referring to Figure 4, it is noted that the PBM performs better in the range of stress factors seen for this application. This validation condition, although only in calendar aging, is the closest experimental condition, since the cycling conditions assume high C-Rates for calibration.

5.3. RegA Frequency Regulation

The characteristics of the RegA profile have been previously explored in detail in Section 4. Figure 8 shows that the battery packs are subjected to continuous, low amplitude current demands and operate around mean zero current to satisfy the mission profile. Figure 13c shows the results under these operating conditions. It is noted that battery pack replacement is not required in this application and that the degradation phenomena are affected by the ambient temperature variation, exhibited by an oscillating capacity and power fade. The divergence in capacity fade prediction is exclusively attributed to the model structures, and the difference in capacity fade prediction over 3 years is lower than the DCFC case. The first life simulation has a higher capacity loss due to SEI growth, as seen in Figure 4, and the trajectory of the degradation in its second life may involve saturated SEI growth. This trait is captured by the PBM, which shows a saturated \sqrt{time} dependence and predicts a capacity degradation rate of 0.7%/year, whereas the EM showcases the linear portion of the exponential curve at low severity factors (explained in Section 3), since the EM cannot account for the change in degradation rate in its second life. The power fade estimation is calculated with the PBM as well as EM individually in this case. The trend shown by the power fade estimation is observed to be very similar to their capacity fade model counterparts. The power fade estimation by the PBM tracks the SEI layer resistance (thickness), which also affects the capacity loss due to SEI. Thus, the trend observed for the capacity loss and the resistance rise is similar for the PBM. The validation conditions for the RegA profile are similar to those reported for the RegD profile. Again, the performance of the PBM is expected to be better than the EM, considering the validation case under moderate SoC and temperature conditions.

6. Conclusions

Based on the numerical results of case studies, key differences in aging factors and the capabilities and limitations of each model are reported in this paper. The availability of experimental data for calibration and validation of these two models is observed to have a profound effect on their estimation performance, even if calibrated using the same experimental data. The results show that the physics-based model tends to be dependent on the number and/or type of degradation mechanism being modeled, whereas the empirical model is heavily reliant on the type of experimental aging data used for the calibration. This work shows the importance of model selection and the related data requirements for calibration in avoiding misleading results using these models. In particular, the RUL parameter is heavily affected by the model specification due to the limited range of operation of the batteries in SoC, temperature, and SoH. The other important key takeaway from this work is that in several of the grid-connected applications, calendar aging is a fundamental aspect to consider due to the energy-to-power ratio of the application. The lack of exhaustive experimental data for calendar aging can heavily limit the performance of the models. In the specific case analyzed in this work, the limited experimental data in the region of SoH capacity between 90% and 70% for aging conditions make validation difficult. Here, both the capacity and power fade need to be considered, since for high power applications, such as frequency regulation, the increase in resistance can lead to a higher replacement rate. In this study, the focus is restricted to single-battery chemistry (LMO-NMC/GIC), but a similar comparison may be derived for different chemistries as well, showcasing pertinent degradation mechanisms and the ability of each model to capture them.

A critical comparison in second-life applications points out differences in the expected RUL, overall system design, and replacement rate of BESSs. Thus, in the authors' opinion, this analysis, along with the simulation, can help SLB system designers to understand the strengths and weaknesses of using different categories of aging models by simulating various case studies and operational demands.

Author Contributions: Conceptualization, S.V.G. and M.D.; methodology, S.V.G. and M.D.; software, S.V.G.; validation, S.V.G. and M.D.; formal analysis, S.V.G. and M.D.; data curation, S.V.G. and M.D.; writing—original draft preparation, S.V.G. and M.D.; writing—review and editing, S.V.G. and M.D.; supervision, M.D.; project administration, M.D.; funding acquisition, M.D. All authors have read and agreed to the published version of the manuscript.

Funding: This research was funded by the Ford Alliance program.

Conflicts of Interest: The authors declare no conflict of interest.

Abbreviations

The following abbreviations are used in this manuscript:

ζ	Cell capacity or internal resistance at nominal conditions (Ah or Ohm)
α	Time dependent factor
n	Order of the reaction
k_{tot}	Total degradation rate
k_{cal}	Calendar aging degradation rate
k_{cyc}	Cycling aging degradation rate
T	Absolute temperature (K)
SoC_{min}	Lower limit of SoC
SoC_{max}	Upper limit of SoC
I	Applied current (Amps)
I_0	Non-dimensional current correction (Amps) [28]
R	Ideal gas constant ($Jmol^{-1} K^{-1}$)
t	Time
$j_n(t)$	Current density (Am^{-2})

$R_{ct,i}$	Charge transfer resistance at the electrode ($i = p, n$) (Ohm)
R_{ohmic}	Ohmic resistance contribution from electrolyte (Ohm)
$Q_{Li,loss}$	Capacity loss from loss in lithium inventory (Ah)
S_n	Electroactive surface area at the anode (m^2)
Q_{SEI}, Q_{AM}	Capacity loss due to SEI layer growth, LAM (Ah)
Q_{nom}	Nominal capacity (Ah)
ΔR_{SC}	Semi-circle resistance contributions in EIS [27] (Ohm)

Appendix A. Model Calibration

Appendix A.1. Semi-Empirical Physics-Based Model Calibration

The PBM, derived in [26], comprises of the simultaneous estimation of capacity loss, which is subdivided into loss due to the SEI layer and LAM sub-models, and the rise of internal impedance due to SEI layer growth.

The SEI layer growth model utilizes the generalized irreversible side reaction mechanism first proposed by [33], which involves solvent reduction, leading to organic and inorganic Li salt formation and hence increased SEI thickness. The current density (i_s) associated with the irreversible side reaction is governed by interfacial reaction kinetics, using the Butler–Volmer (BV) expression. Therefore, this current density controls the rate of capacity loss through SEI layer growth (Q_{SEI}), given by Figure 2. This irreversible side reaction has an open circuit potential of 0.4 V vs. Li/Li⁺ [26] for the solvent reduction reaction and it is also assumed that solvent reduction can occur only during charging. The model assumes the diffusion of the solvent through the SEI layer to be the limiting factor for the side reaction and that the concentrations in the bulk and at the surface of the active material are equal. The solvent reduction reaction is also considered irreversible [33] and thus a cathodic Tafel approximation is used to simplify the model. The empirical parameter ζ as reported in [26], which assumes an isothermally constant exchange current density, is modified by [45] to include an Arrhenius relationship since there exists a rate constant dependence on temperature.

The structural changes caused by constant cycling of Li ions result in either partial or complete isolation of active material sites, making them inaccessible for Li ions and therefore reducing the effective cell capacity. From [62], we discern that the rate of capacity loss is directly proportional to the rate of change of active material and the degree of lithiation of the lost lithium when the loss of active material site occurs. The LAM sub-model utilizes the SoC as a stress factor in estimating the lithium loss (capacity loss) due to the active material, and the rate of change of the active material is not affected by the degree of lithiation. Since the interaction of loss of active material sites and the lithium inventory are interlinked, the dependence of the rate of change of active material volume fraction on the degree of lithiation (measure of the SoC) becomes crucial. A modification of the expression in [26] presented in [45] allows the LAM sub-model to become dependent on the remaining Li inventory with non-linear capacity loss seen at higher aggregated Ah throughput.

For the power fade model, there are several different contributions to the total resistance in Equation (8), given by electrical, thermal, and kinetic phenomena as well as through side reactions (SEI layer) [27]. The ohmic resistance contribution is given by the electrolytic resistance in [27], but may also include the contact resistances of the collectors while measuring the cell voltage. The kinetic contributions include the charge transfer resistances in the positive and negative electrodes. The change in thickness of the SEI layer corresponds to a rise in resistivity for the SEI layer, which is given by Equation (9). The SEI layer parameters are generally assumed from the literature [27] for the molar mass of the SEI layer; the M_{SEI} is equal to 16.2 kgmol^{-1} and the density of the SEI layer, ρ_{SEI} , is equal to 1690 kgm^{-3} . However, the value of ionic conductivity in the SEI layer, κ_{SEI}^* , ranges from 1 to $1 \times 10^{-7} \text{ S/m}$ in the literature [63,64].

One of the primary mechanisms of capacity fade, i.e., SEI growth, is also seen a major contributor to the power fade in a cell. While the LAM in cathode materials with transition metals can trigger an increased capacity fade, it has also been known to accelerate the rate of SEI formation in [36,57] and thus increase the power fade. It is fundamental to understand the variation in internal resistance with aging, and within the context of this study, the power fade model is required to work in tandem with the physics-based capacity fade model. To the best of the authors' knowledge, the evolution of ohmic and charge transfer resistance contributions with aging (also, in second-life applications) has not been investigated in detail in the literature. Thus, the modeling impedance rise due to SEI layer growth is assumed as the primary variation in resistance for our case, thereby we neglect the change in charge transfer resistance and ohmic drop in the electrolyte with aging. The complexity involved in modeling transition metal dissolution and active material loss in the cathode has led us to this supposition.

Appendix A.2. Electrochemical Performance Model Calibration

Starting from the extended single particle model (ESPM) proposed in [52] for 15 Ah LMO-NMC chemistry cells, the kinetic, ohmic, and transport parameters were tuned with multiple experiments carried out on LMO-NMC battery packs. The considered experimental datasets include a C/10 discharge test and an RCID test (multiple charge/discharge pulses at different C-rates at each SoC point), both conducted at 25 °C. The slow discharge test is useful for fine tuning the lithiation range as well as the open circuit potential of each electrode and the RCID test helps in fine tuning transport and ohmic parameters with short transients.

Table A1. Electrochemical model-tuned anode parameters in solid and liquid phases.

Electrochemical Model Parameters	Values	Units
Anode diffusion coefficient	$0.5 \cdot 10^{-14}$	m ² /s
Anode density	2250	kg/m ³
Anode specific capacity	372	Ah/kg
Anode particle radius	$3.5 \cdot 10^{-6}$	m
Anode thickness	$5 \cdot 10^{-5}$	m
Anode active material volume fraction	0.53	-
Anode rate constant	$7 \cdot 10^{-10}$	mol/ m ² ·s
x0—fully delithiated anode	0.01	V
xf—fully lithiated anode	0.8617	V
Liquid diffusion coefficient	$0.49 \cdot 10^{-10}$	m ² /s
Nominal electrolyte concentration	1000	mol/m ³
Activity coefficient in liquid phase	1.75	-
Bruggman coefficient	2.8	-
Transference number	0.39	-
Porosity (anode, separator)	0.46	-

References

1. Bobba, S.; Podias, A.; Di Persio, F.; Messagie, M.; Tecchio, P.; Cusenza, M.A.; Eynard, U.; Mathieux, F.; Pfrang, A. *Sustainability Assessment of Second Life Application of Automotive Batteries (SASLAB)*; JRC Exploratory Research (2016–2017), Final Report; Publications Office of the European Union: Luxembourg, 2018.
2. Shahjalal, M.; Roy, P.K.; Shams, T.; Fly, A.; Chowdhury, J.I.; Ahmed, M.R.; Liu, K. A review on second-life of Li-ion batteries: Prospects, challenges, and issues. *Energy* **2022**, *241*, 122881. [[CrossRef](#)]
3. Hunt, G. *USABC Electric Vehicle Battery Test Procedures Manual*; United States Department of Energy: Washington, DC, USA, 1996.
4. Goebel, K.; Saha, B.; Saxena, A.; Celaya, J.R.; Christophersen, J.P. Prognostics in battery health management. *IEEE Instrum. Meas. Mag.* **2008**, *11*, 33–40. [[CrossRef](#)]

5. Onori, S.; Spagnol, P.; Marano, V.; Guezennec, Y.; Rizzoni, G. A new life estimation method for lithium-ion batteries in plug-in hybrid electric vehicles applications. *Int. J. Power Electron.* **2012**, *4*, 302–319. [\[CrossRef\]](#)
6. Xing, Y.; Williard, N.; Tsui, K.L.; Pecht, M. A comparative review of prognostics-based reliability methods for lithium batteries. In Proceedings of the 2011 Prognostics and System Health Management Conference, Shenzhen, China, 24–25 May 2011; pp. 1–6.
7. Smith, K.; Warleywine, M.; Wood, E.; Neubauer, J.; Pesaran, A. *Comparison of Plug-In Hybrid Electric Vehicle Battery Life across Geographies and Drive-Cycles*; Technical Report; National Renewable Energy Lab. (NREL): Golden, CO, USA, 2012.
8. Haram, M.H.S.M.; Lee, J.W.; Ramasamy, G.; Ngu, E.E.; Thiagarajah, S.P.; Lee, Y.H. Feasibility of utilising second life EV batteries: Applications, lifespan, economics, environmental impact, assessment, and challenges. *Alex. Eng. J.* **2021**, *60*, 4517–4536. [\[CrossRef\]](#)
9. Jiao, N.; Evans, S. Business models for sustainability: The case of second-life electric vehicle batteries. *Procedia Cirp* **2016**, *40*, 250–255. [\[CrossRef\]](#)
10. Hossain, E.; Murtaugh, D.; Mody, J.; Faruque, H.M.R.; Sunny, M.S.H.; Mohammad, N. A Comprehensive Review on Second-Life Batteries: Current State, Manufacturing Considerations, Applications, Impacts, Barriers & Potential Solutions, Business Strategies, and Policies. *IEEE Access* **2019**, *7*, 73215–73252.
11. D’Arpino, M.; Cancian, M. *Design of a Grid-Friendly dc Fast Charge Station with Second Life Batteries*; Technical Report, SAE Technical Paper; SAE: Warrendale, PA, USA, 2019.
12. Martinez-Laserna, E.; Gandiaga, I.; Sarasketa-Zabala, E.; Badedo, J.; Stroe, D.I.; Swierczynski, M.; Goikoetxea, A. Battery second life: Hype, hope or reality? A critical review of the state of the art. *Renew. Sustain. Energy Rev.* **2018**, *93*, 701–718. [\[CrossRef\]](#)
13. Zhao, Y.; Pohl, O.; Bhatt, A.I.; Collis, G.E.; Mahon, P.J.; Rütther, T.; Hollenkamp, A.F. A Review on Battery Market Trends, Second-Life Reuse, and Recycling. *Sustain. Chem.* **2021**, *2*, 167–205. [\[CrossRef\]](#)
14. White, C.; Thompson, B.; Swan, L.G. Repurposed electric vehicle battery performance in second-life electricity grid frequency regulation service. *J. Energy Storage* **2020**, *28*, 101278. [\[CrossRef\]](#)
15. Li, H.; Alsolami, M.; Yang, S.; Alsmadi, Y.M.; Wang, J. Lifetime test design for second-use electric vehicle batteries in residential applications. *IEEE Trans. Sustain. Energy* **2017**, *8*, 1736–1746. [\[CrossRef\]](#)
16. Faisal, M.; Hannan, M.A.; Ker, P.J.; Hussain, A.; Mansor, M.B.; Blaabjerg, F. Review of energy storage system technologies in microgrid applications: Issues and challenges. *IEEE Access* **2018**, *6*, 35143–35164. [\[CrossRef\]](#)
17. Fan, X.; Liu, B.; Liu, J.; Ding, J.; Han, X.; Deng, Y.; Lv, X.; Xie, Y.; Chen, B.; Hu, W.; et al. Battery technologies for grid-level large-scale electrical energy storage. *Trans. Tianjin Univ.* **2020**, *26*, 92–103. [\[CrossRef\]](#)
18. Abronzini, U.; Attaianesi, C.; D’Arpino, M.; Di Monaco, M.; Tomasso, G. Cost minimization energy control including battery aging for multi-source ev charging station. *Electronics* **2019**, *8*, 31. [\[CrossRef\]](#)
19. Deng, Y.; Zhang, Y.; Luo, F. Operational planning of centralized charging stations using second-life battery energy storage systems. *IEEE Trans. Sustain. Energy* **2020**, *12*, 387–399. [\[CrossRef\]](#)
20. Braco, E.; San Martín, I.; Berrueta, A.; Sanchis, P.; Ursúa, A. Experimental assessment of cycling ageing of lithium-ion second-life batteries from electric vehicles. *J. Energy Storage* **2020**, *32*, 101695. [\[CrossRef\]](#)
21. Coron, E.; Geniès, S.; Cugnet, M.; Thivel, P. Impact of Lithium-Ion Cell Condition on Its Second Life Viability. *J. Electrochem. Soc.* **2020**, *167*, 110556. [\[CrossRef\]](#)
22. Mathews, I.; Xu, B.; He, W.; Barreto, V.; Buonassisi, T.; Peters, I.M. Technoeconomic model of second-life batteries for utility-scale solar considering calendar and cycle aging. *Appl. Energy* **2020**, *269*, 115127. [\[CrossRef\]](#)
23. Jin, X.; Vora, A.; Hoshing, V.; Saha, T.; Shaver, G.; Wasynczuk, O.; Varigonda, S. Applicability of available Li-ion battery degradation models for system and control algorithm design. *Control Eng. Pract.* **2018**, *71*, 1–9. [\[CrossRef\]](#)
24. Xiong, R.; Pan, Y.; Shen, W.; Li, H.; Sun, F. Lithium-ion battery aging mechanisms and diagnosis method for automotive applications: Recent advances and perspectives. *Renew. Sustain. Energy Rev.* **2020**, *131*, 11004. [\[CrossRef\]](#)
25. Vermeer, W.; Mouli, G.R.C.; Bauer, P. A comprehensive review on the characteristics and modeling of lithium-ion battery aging. *IEEE Trans. Transp. Electrification* **2021**, *8*, 2205–2232. [\[CrossRef\]](#)
26. Jin, X.; Vora, A.; Hoshing, V.; Saha, T.; Shaver, G.; García, R.E.; Wasynczuk, O.; Varigonda, S. Physically-based reduced-order capacity loss model for graphite anodes in Li-ion battery cells. *J. Power Sources* **2017**, *342*, 750–761. [\[CrossRef\]](#)
27. Prada, E.; Di Domenico, D.; Creff, Y.; Bernard, J.; Sauvant-Moynot, V.; Huet, F. A simplified electrochemical and thermal aging model of LiFePO₄-graphite Li-ion batteries: Power and capacity fade simulations. *J. Electrochem. Soc.* **2013**, *160*, A616–A628. [\[CrossRef\]](#)
28. Baghdadi, I.; Briat, O.; Delétage, J.Y.; Gyan, P.; Vinassa, J.M. Lithium battery aging model based on Dakin’s degradation approach. *J. Power Sources* **2016**, *325*, 273–285. [\[CrossRef\]](#)
29. Birkl, C.R.; Roberts, M.R.; McTurk, E.; Bruce, P.G.; Howey, D.A. Degradation diagnostics for lithium ion cells. *J. Power Sources* **2017**, *341*, 373–386. [\[CrossRef\]](#)
30. Lu, L.; Han, X.; Li, J.; Hua, J.; Ouyang, M. A review on the key issues for lithium-ion battery management in electric vehicles. *J. Power Sources* **2013**, *226*, 272–288. [\[CrossRef\]](#)
31. D’Arpino, M.; Cancian, M. Lifetime Optimization for a Grid-Friendly DC Fast Charge Station with Second Life Batteries. *ASME Lett. Dyn. Syst. Control.* **2021**, *1*, 011014. [\[CrossRef\]](#)
32. Cordoba Arenas, A.C. Aging Propagation Modeling and State-of-Health Assessment in Advanced Battery Systems. Ph.D. Thesis, The Ohio State University, Columbus, OH, USA, 2013.

33. Ramadass, P.; Haran, B.; Gomadam, P.M.; White, R.; Popov, B.N. Development of first principles capacity fade model for Li-ion cells. *J. Electrochem. Soc.* **2004**, *151*, A196–A203. [[CrossRef](#)]
34. Safari, M.; Morcrette, M.; Teysot, A.; Delacourt, C. Multimodal physics-based aging model for life prediction of Li-ion batteries. *J. Electrochem. Soc.* **2009**, *156*, A145–A153. [[CrossRef](#)]
35. Pinson, M.B.; Bazant, M.Z. Theory of SEI formation in rechargeable batteries: Capacity fade, accelerated aging and lifetime prediction. *J. Electrochem. Soc.* **2013**, *160*, A243–A250. [[CrossRef](#)]
36. Kindermann, F.M.; Keil, J.; Frank, A.; Jossen, A. A SEI modeling approach distinguishing between capacity and power fade. *J. Electrochem. Soc.* **2017**, *164*, E287–E294. [[CrossRef](#)]
37. Dubarry, M.; Liaw, B.Y.; Chen, M.S.; Chyan, S.S.; Han, K.C.; Sie, W.T.; Wu, S.H. Identifying battery aging mechanisms in large format Li ion cells. *J. Power Sources* **2011**, *196*, 3420–3425. [[CrossRef](#)]
38. Mao, Z.; Farkhondeh, M.; Pritzker, M.; Fowler, M.; Chen, Z. Calendar aging and gas generation in commercial graphite/NMC-LMO lithium-ion pouch cell. *J. Electrochem. Soc.* **2017**, *164*, A3469–A3483. [[CrossRef](#)]
39. Zhao, X.; Yin, Y.; Hu, Y.; Choe, S.Y. Electrochemical-thermal modeling of lithium plating/stripping of $\text{Li}(\text{Ni}_{0.6}\text{Mn}_{0.2}\text{Co}_{0.2})\text{O}_2$ /Carbon lithium-ion batteries at subzero ambient temperatures. *J. Power Sources* **2019**, *418*, 61–73. [[CrossRef](#)]
40. Hu, X.; Zhang, K.; Liu, K.; Lin, X.; Dey, S.; Onori, S. Advanced Fault Diagnosis for Lithium-Ion Battery Systems. *IEEE Ind. Electron. Mag.* **2020**, *14*, 65–91. [[CrossRef](#)]
41. Lipu, M.H.; Hannan, M.; Hussain, A.; Hoque, M.; Ker, P.J.; Saad, M.H.M.; Ayob, A. A review of state of health and remaining useful life estimation methods for lithium-ion battery in electric vehicles: Challenges and recommendations. *J. Clean. Prod.* **2018**, *205*, 115–133. [[CrossRef](#)]
42. Lin, C.; Tang, A.; Wang, W. A review of SOH estimation methods in Lithium-ion batteries for electric vehicle applications. *Energy Procedia* **2015**, *75*, 1920–1925. [[CrossRef](#)]
43. Safari, M.; Delacourt, C. Modeling of a commercial graphite/LiFePO₄ cell. *J. Electrochem. Soc.* **2011**, *158*, A562–A571. [[CrossRef](#)]
44. Naumann, M.; Schimpe, M.; Keil, P.; Hesse, H.C.; Jossen, A. Analysis and modeling of calendar aging of a commercial LiFePO₄/graphite cell. *J. Energy Storage* **2018**, *17*, 153–169. [[CrossRef](#)]
45. Salyer, Z.; D’Arpino, M.; Canova, M. Extended Physics-Based Reduced-Order Capacity Fade Model for Lithium-Ion Battery Cells. *ASME Lett. Dyn. Syst. Control* **2021**, *1*, 041002. [[CrossRef](#)]
46. Gyan, P.; Aubret, P.; Hafsaoui, J.; Sellier, F.; Bourlot, S.; Zinola, S.; Badin, F. Experimental assessment of battery cycle life within the SIMSTOCK research program. *Oil Gas Sci. Technol.-D’IFP Energies Nouv.* **2013**, *68*, 137–147. [[CrossRef](#)]
47. Cordoba-Arenas, A.; Onori, S.; Guezennec, Y.; Rizzoni, G. Capacity and power fade cycle-life model for plug-in hybrid electric vehicle lithium-ion battery cells containing blended spinel and layered-oxide positive electrodes. *J. Power Sources* **2015**, *278*, 473–483. [[CrossRef](#)]
48. Belt, J.; Utgikar, V.; Bloom, I. Calendar and PHEV cycle life aging of high-energy, lithium-ion cells containing blended spinel and layered-oxide cathodes. *J. Power Sources* **2011**, *196*, 10213–10221. [[CrossRef](#)]
49. Sadabadi, K.K.; Jin, X.; Rizzoni, G. Prediction of remaining useful life for a composite electrode lithium ion battery cell using an electrochemical model to estimate the state of health. *J. Power Sources* **2021**, *481*, 228861. [[CrossRef](#)]
50. Schmalstieg, J.; Käbitz, S.; Ecker, M.; Sauer, D.U. A holistic aging model for Li (NiMnCo)O₂ based 18650 lithium-ion batteries. *J. Power Sources* **2014**, *257*, 325–334. [[CrossRef](#)]
51. Ganesh, S.V. Critical Analysis of Aging Models for Lithium-Ion Second-Life Battery Applications. Ph.D. Thesis, The Ohio State University, Columbus, OH, USA, 2020.
52. Bartlett, A.P. Electrochemical Model-Based State of Charge and State of Health Estimation of Lithium-Ion Batteries. Ph.D. Thesis, The Ohio State University, Columbus, OH, USA, 2015.
53. Safari, M.; Delacourt, C. Aging of a commercial graphite/LiFePO₄ cell. *J. Electrochem. Soc.* **2011**, *158*, A1123–A1135. [[CrossRef](#)]
54. Liu, W.; Delacourt, C.; Forgez, C.; Pelissier, S. Study of graphite/NCA Li-ion cell degradation during accelerated aging tests—Data analysis of the SIMSTOCK project. In Proceedings of the 2011 IEEE Vehicle Power and Propulsion Conference, Chicago, IL, USA, 6–9 September 2011; pp. 1–6.
55. Grolleau, S.; Delaille, A.; Gualous, H.; Gyan, P.; Revel, R.; Bernard, J.; Redondo-Iglesias, E.; Peter, J.; Network, S. Calendar aging of commercial graphite/LiFePO₄ cell—Predicting capacity fade under time dependent storage conditions. *J. Power Sources* **2014**, *255*, 450–458. [[CrossRef](#)]
56. Delaille, A.; Grolleau, S.; Duclaud, F.; Bernard, J.; Revel, R.; Pelissier, S.; Redondo-Iglesias, E.; Vinassa, J.M.; Eddahech, A.; Forgez, C.; et al. *SIMCAL Project: Calendar Aging Results Obtained on a Panel of 6 Commercial Li-Ion Cells*; The Electrochemical Society: Pennington, NJ, USA, 2013.
57. Gilbert, J.A.; Shkrob, I.A.; Abraham, D.P. Transition metal dissolution, ion migration, electrocatalytic reduction and capacity loss in lithium-ion full cells. *J. Electrochem. Soc.* **2017**, *164*, A389–A399. [[CrossRef](#)]
58. Battaglia, D.; D’Arpino, M.; Ganesh, S.V.; Carlson, J. Impact of power profile on the estimation of second life batteries remaining useful life. *SAE Int. J. Adv. Curr. Pract. Mobil.* **2021**, *3*, 2906–2914.
59. Gohla-Neudecker, B.; Bowler, M.; Mohr, S. Battery 2 nd life: Leveraging the sustainability potential of EVs and renewable energy grid integration. In Proceedings of the 2015 International Conference on Clean Electrical Power (ICCEP 2015), Taormina, Italy, 16–18 June 2015; pp. 311–318.

60. D'Arpino, M.; Singh, G.; Koh, M.B. *Impact of Event-Based EV Charging Power Profile on Design and Control of Multi-Source DCFC Stations*; Technical Report, SAE Technical Paper; SAE: Warrendale, PA, USA, 2023.
61. Palizban, O.; Kauhaniemi, K. Energy storage systems in modern grids—Matrix of technologies and applications. *J. Energy Storage* **2016**, *6*, 248–259. [[CrossRef](#)]
62. Kalupson, J.; Luo, G.; Shaffer, C.E. *AutoLion™: A Thermally Coupled Simulation Tool for Automotive Li-Ion Batteries*; Technical Report, SAE Technical Paper; SAE: Warrendale, PA, USA, 2013.
63. Ning, G.; White, R.E.; Popov, B.N. A generalized cycle life model of rechargeable Li-ion batteries. *Electrochim. Acta* **2006**, *51*, 2012–2022. [[CrossRef](#)]
64. Ramasamy, R.P.; Lee, J.W.; Popov, B.N. Simulation of capacity loss in carbon electrode for lithium-ion cells during storage. *J. Power Sources* **2007**, *166*, 266–272. [[CrossRef](#)]

Disclaimer/Publisher's Note: The statements, opinions and data contained in all publications are solely those of the individual author(s) and contributor(s) and not of MDPI and/or the editor(s). MDPI and/or the editor(s) disclaim responsibility for any injury to people or property resulting from any ideas, methods, instructions or products referred to in the content.